Time-resolved photon migration in bi-layered tissue models

Karthik Vishwanath[1] and Mary-Ann Mycek[1,2,3]

[1]Department of Biomedical Engineering, [2]Comprehensive Cancer Center, [3]Applied Physics Program
University of Michigan, Ann Arbor, MI 48109-2099
mycek@umich.edu

Abstract: In this article, we describe a novel Monte Carlo code for time-integrated and time-resolved photon migration simulations of excitation and fluorescent light propagation (with reabsorption) in bi-layered models of biological tissues. The code was experimentally validated using bi-layered, tissue-simulating phantoms and the agreement between simulations and experiment was better than 3%. We demonstrate the utility of the code for quantitative clinical optical diagnostics in epithelial tissues by examining design characteristics for clinically compatible waveguides with arbitrarily complex source-detector configurations. Results for human colonic tissues included a quantitative comparison of simulation predictions with time-resolved fluorescence data measured *in vivo* and spatio-temporal visualizations of photon migration characteristics in tissue models in both two- and three-dimensions for source-detector configurations, including variable waveguide spacing, numerical aperture, and diameter. These results were then extended from surface point spectroscopy to imaging modalities for both time-gated (fluorescence lifetime) and steady-state (fluorescence intensity) experimental conditions. To illustrate the flexibility of this computational approach, time-domain results were extended to simulate predictions for frequency-domain instrumentation. This work is the first demonstration and validation of a time-domain, multi-wavelength photon transport model with these capabilities in layered turbid-media.

OCIS Codes: (170.6510) Spectroscopy, tissue diagnostics; (170.3650) Lifetime-based sensing; (170.3660) Light propagation in tissues; (170.6280) Spectroscopy, fluorescence and luminescence

References and Links

1. M.-A. Mycek and B.W. Pogue, eds. Handbook of biomedical fluorescence.(Marcel Dekker, Inc., 2003)
2. F. Koenig, F. Mcgovern, A. Althausesn, T. Deutsch, and K. Schomacker, "Laser induced autofluorescence diagnosis of bladder cancer," J. Urol. **156,** 1597-1602 (1996)
3. M.-A. Mycek, K. Schomacker, and N. Nishioka, "Colonic polyp differentiation using time resolved autofluorescence spectroscopy," Gastrointestinal Endoscopy **48,** 390-394 (1998)
4. K.T. Schomacker, J.K. Frisoli, C.C. Compton, T.J. Flotte, J.M. Richter, N.S. Nishioka, and T.F. Deutsch, "Ultraviolet laser-induced fluorescence of colonic tissue: Basic biology and diagnostic potential," Lasers Surg. Med. **12,** 63-78 (1992)
5. N. Ramanujam, A. Mahadevan, M. Follen-Mitchell, S. Thomsen, E. Silva, and R. Richards-Kortum, "Fluorescence spectroscopy of the cervix," Clinical Consultations in Obstetrics and Gynecology **6,** 62-69 (1994)
6. S. Lam, C.J. Macaulay, C. Leriche, N. Ikeda, and B. Palcic, "Early localization of bronchogenic carcinoma," Diagnostic and Therapeutic Endoscopy **1,** 75-78 (1994)
7. H. Yokomise, K. Yanagihara, T. Fukuse, T. Hirata, O. Ike, H. Mizuno, H. Wada, and S. Hitomi, "Clinical experience with lung-imaging fluorescence endoscope (life) in patients with lung cancer," J. Bronchology **4,** 205-208 (1997)
8. T.D. Wang, J. Van-Dam, J.M. Crawford, E.A. Preisinger, Y. Wang, and M.S. Feld, "Fluorescence endoscopic imaging of human colonic adenomas," Gastroenterology **111,** 1182-1191 (1996)

#8207 - $15.00 USD Received 19 July 2005; revised 2 September 2005; accepted 7 September 2005

9. B. Chwirot, S. Chwirot, W. Jedrzejczyk, M. Jackowski, A. Raczynska, J. Winczakiewicz, and J. Dobber, "Ultraviolet laser-induced fluorescence of human stomach tissues: Detection of cancer tissues by imaging techniques," Lasers Surg. Med. **21,** 149-158 (1997)
10. R.S. Dacosta, B.C. Wilson, and N.E. Marcon, "Light-induced fluorescence endoscopy of the gastrointestinal tract," Gastrointestinal Endoscopy **10,** 37-69 (2000)
11. H. Zeng, C. Macaulay, D.I. Mclean, and B. Palcic, "Reconstruction of in vivo skin autofluorescence spectrum from microscopic properties by monte carlo simulation," J. Photochem. Photobiol. **38,** 234-240 (1997)
12. K. Rinzema, L.H.P. Murrer, and W.M. Star, "Direct experimental verification of light transport theory in an optical phantom," J. Opt. Soc. Am. A **15,** 2078-2088 (1998)
13. K. Vishwanath, B.W. Pogue, and M.-A. Mycek, "Quantitative fluorescence lifetime spectroscopy in turbid media: Comparison of theoretical, experimental and computational methods," Phys. Med. Biol. **47,** 3387-3405 (2002)
14. D. Hidovic-Rowe and E. Claridge, "Modeling and validation of spectral reflectance for the colon," Phys. Med. Biol. **50,** 1071-1093 (2005)
15. A.J. Welch and M.J.C. Van-Gemert, *Optical-thermal response of laser-irradiated tissue*, (Plenum Press, New York, 1995)
16. K. Vishwanath "Computational modeling of time-resolved fluorescence transport in turbid media for non-invasive clinical diagnostics," Ph.D. (University of Michigan, Ann Arbor, 2005)
17. L. Wang, S.L. Jacques, and L. Zheng, "Mcml - monte carlo modeling of photon transport in multi-layered tissues," Comput Methods Programs Biomed **47,** 131-146 (1995)
18. S.L. Jacques, "Time resolved propagation of ultrashort laser pulses within turbid tissue.," Appl. Opt. 28, 2223-2229 (1989)
19. B.W. Pogue and G. Burke, "Fiber-optic bundle design for quantitative fluorescence measurement from tissue," Appl. Opt. **37,** 7429 - 7436 (1998)
20. K. Vishwanath and M.-A. Mycek, "Do fluorescence decays remitted from tissues accurately reflect intrinsic fluorophore lifetimes?," Opt. Lett. **29,** 1512-1514 (2004)
21. J. Valenzuela, K. Vishwanath, and M.-A. Mycek."Designing optical waveguides for clinical diagnostics in layered tissues: Experimental testing with tissue phantoms," in IEEE Conference on Lasers and Electro-Optics (LEOS), **1,** 827-829 (2004)
22. A. Sefkow, M. Bree, and M.-A. Mycek, "A method for measuring cellular optical absorption and scattering evaluated using dilute cell suspension phantoms.," Appl. Spectrosc. **55,** 1495-1501 (2001)
23. J.D. Pitts and M.-A. Mycek, "Design and development of a rapid acquisition laser-based fluorometer with simultaneous spectral and temporal resolution.," Rev. Sci. Instrum. **72,** 3061-3072 (2001)
24. T.J. Pfefer, L.S. Matchette, A.M. Ross, and M.N. Ediger, "Selective detection of fluorophore layers in turbid media: The role of fiber-optic probe design," Opt. Lett. **28,** 120-122 (2003)
25. E. Kuwana and E.M. Sevick-Muraca, "Fluorescence lifetime spectroscopy in multiply scattering media with dyes exhibiting multiexponential decay kinetics," Biophys. J. **83,** 1165-1176 (2002)

1. Introduction

Methods of optical science and engineering are being developed for a variety of applications in biomedical therapeutics and diagnostics. Fluorescence techniques represent an important class of optical methods being applied to *in vitro* and *in vivo* biomedical diagnostics, including noninvasive molecular sensing and imaging [1]. Fluorescence methods are useful in biomedical research, including *in vivo* studies, for several reasons, including the molecular specificity and functional sensitivity of the technique, the relatively large signal strength in regions of the electromagnetic spectrum readily accessible to experimentalists, and the many bio-compatible fluorophores (endogenous and exogenous) available for study. Because fluorescence spectroscopy may be performed with thin, flexible, fiber-optic waveguides, the technique is clinically feasible and allows access to internal organs endoscopically or surgically [2-5]. Fluorescence spectroscopy methods may be adapted to an imaging modality, enabling physicians to examine larger areas of tissue with spectroscopic sensitivity [6-10].

Measured tissue fluorescence signals reflect both intrinsic tissue pathology (local morphological, biochemical, and optical properties), as well as experimental design features (including excitation and emission wavelengths, fiber-optic probe design, and contrast agent concentration). Computational methods are often employed to quantitatively simulate photon migration characteristics in tissues, thereby enabling accurate analysis and interpretation of measured tissue fluorescence signals [11-14]. Further, such numerical approaches can be employed to computationally engineer optical instrumentation designs that are optimized for specific applications in clinical spectroscopy and imaging, while restricting costly and time-consuming experimental fabrication and testing to only those designs most likely to succeed.

#8207 - $15.00 USD Received 19 July 2005; revised 2 September 2005; accepted 7 September 2005

Here, we describe a novel Monte Carlo code for time-integrated and time-resolved photon migration simulations of excitation and fluorescent light propagation in bi-layered models of biological tissues. We validate the code experimentally and present results to illustrate its utility for quantitative clinical optical diagnostics in human epithelial tissues.

2. Materials and methods

2.1. Monte Carlo model for bi-layered media

Light transport in optically scattering and absorbing media, such as biological tissues, has been modeled successfully by Monte Carlo techniques, which have provided the most accurate descriptions of light distribution in these inhomogeneous, turbid media [1, 15]. As described previously [13, 16], the photons paths consist of steps of variable sizes that are sampled via an exponential probability density distribution of the path length, as determined by the medium's scattering coefficient (μ_s). Each photon begins its flight with a weight of unity, which is attenuated after each step as determined by the medium's absorption coefficient (μ_a) following Beer's law. After each scattering step, a new direction for the photon trajectory is calculated via the scattering phase function (the Henyey-Greenstein function [17]), which is specified by the anisotropy coefficient (g) of the tissue. The flight of the photon ends when it leaves the tissue (by crossing the tissue-air interface) or when its weight falls below a threshold minimum value (set to $1x10^{-5}$), as determined by a Russian roulette routine [17]. At the end of its travel in the tissue, the time, t, spent by the photon inside the medium is given by $t=L/nc$, where L is the total path-length of the photon in the medium, c is the speed of light in vacuum, and n is the refractive index of the medium [18].

For fluorescence modeling, each photon begins its flight as an excitation photon. Fluorescence absorption is sampled using a rejection technique, after each scattering event of the excitation photon, as governed by the coefficient of fluorophore absorption at the excitation wavelength, μ_{afx} [19]. Upon successful fluorescence absorption, the excitation photon is relabeled as a fluorescence photon, where its new direction of travel is determined by an isotropic scattering event and its weight is multiplied by the fluorescence quantum yield, Φ_{QY}. This newly created fluorescence photon then continues to propagate from the point of its spatial origin, as governed by the scattering, absorption, and anisotropy coefficients of the medium at the fluorescence emission wavelength. After each successful fluorescence absorption event the simulation adds a sampled decay time, t_d, to the photon's total time of flight to include the effect of a finite fluorophore lifetime (τ_0) [13]. It is to be noted that the simulation tracks the optical transport properties of each layer, separately, for all possible photon wavelengths. (The total number of possible photon wavelengths included a single excitation wavelength, as well as all possible emission wavelengths, as defined by the fluorophores specified in the input tissue model.) Thus, it was possible to define fluorophore coefficients to account for the reabsorption of a fluorescence photon (remitted by a fluorophore) to yield another photon at a longer wavelength (remitted by a second, different fluorophore) [16]. The ability to simulate multiple reabsorption effects in a turbid medium makes this model non-conforming to some synthetic techniques that can be employed to speed-up fluorescence Monte Carlo computation times.

Photons are launched into the tissue model at the air-tissue interface via a “source” optical fiber of specified numerical aperture and diameter whose axis is normal to the tissue surface. For both the excitation and fluorescence photons the simulation stores the relative fractional number of photons (with respect to the total photons simulated) escaping the tissue surface per unit time over the surface of the “detector” annuli of mean radius ρ concentric with the source fiber. The simulation also stores the three-dimensional locations of the spatial origin of fluorescence photons that are detected by each detector on the surface of the tissue. Axial tissue inhomogeneity is modeled by stacking turbid layers atop one another, where each layer is specified as a homogeneous medium, characterized by its individual optical transport properties and fluorescence properties as described above [20]. Photon steps crossing layer-layer interfaces or leading to the photon exiting the tissue medium are treated with greater

#8207 - $15.00 USD Received 19 July 2005; revised 2 September 2005; accepted 7 September 2005

care by using the Fresnel reflection coefficient along with Snell's law to determine the photon trajectories across refractive index mismatched layers, as described previously [17].

Figure 1 depicts a schematic view of the geometry of the source-detector configuration examining a bi-layered tissue medium with a layer of finite thickness (z_1) atop a very thick bottom layer ($z_2 \sim \infty$).

2.2. Fluorescent bi-layered tissue phantoms

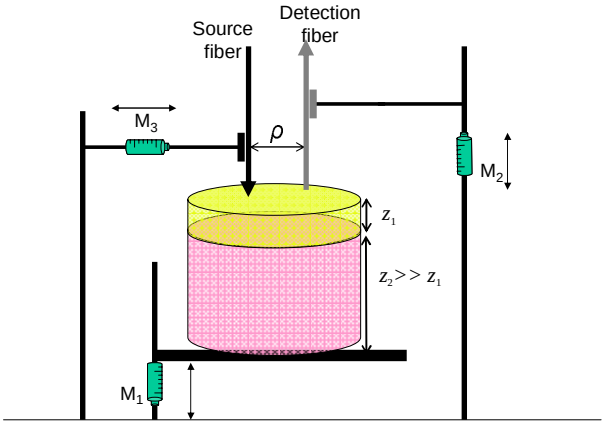

Fig. 1. Apparatus used for accurate control of fiber-optic source-detector positioning relative to the surface of the bi-layered phantom (cylindrical layers at center).

Bi-layered tissue phantoms were constructed to validate Monte Carlo simulations of bi-layered tissue fluorescence. These phantoms were constructed as a two-phase mixture, where each phase represented a different layer in the tissue model. The bi-layered fluorescent medium was composed of a liquid top layer and a solid, hydrophobic bottom layer, as shown schematically in Fig.1 [21]. This design allowed for precise and rapidly variable control of the optical properties in the liquid layer (including layer thickness, fluorophore concentration, and the optical scattering coefficient), while the solid "semi-infinite" bottom layer maintained consistent, fixed optical properties, thereby providing a long-term, reusable bottom layer. The two-phase phantom thus provided a quick and clean method to maintain a sharp boundary between layers, thereby avoiding techniques to create bi-layered phantoms that employed optically uncharacterized thin membranes (such as a plastic wrap) to separate two liquid layers.

The solid bottom layer was made from a transparent high-strength, two component (base and catalyst) silicone polymer (Rhodorsil RTV 141). The base and catalyst were mixed in a 10:1 ratio, by weight. Polystyrene microspheres (Duke Scientific, Cat. No. 4010A) were added to the base such that the microspheres occupied a pre-calculated volume fraction *f*, in the total phantom volume mixture to provide scattering coefficients similar to human colonic tissues [20, 22]. Rhodamine-6G (Sigma, Cat. No. R4127-25G) was dissolved in DI (de-ionized) water and was subsequently added to the base mixture, such that the final concentration of Rhodamine-6G in the mixture was ~5μM. The base, fluorophore, and scattering spheres were then transferred into a Pyrex dish and stirred at a temperature of ~ 70°C on a hot plate for 24-48 hours using a magnetic stirrer, until the mixture appeared homogeneous. The catalyst was then added and the resulting mixture was cured for 24 hours

#8207 - $15.00 USD Received 19 July 2005; revised 2 September 2005; accepted 7 September 2005

in a cool, dark enclosure until it polymerized into a water-resistant solid matrix. The solidified matrix along with the scattering spheres and Rhodamine-6G formed the bottom layer of the bi-layered fluorescent tissue phantom.

To make the top layer, a concentrated POPOP (1,4-bis(5-phenyloxazol-2-yl) benzene) solution (~0.1 mM) (Sigma, Cat. No. P-3754) in ethanol was diluted to a lower concentration (~10 μM) by adding calculated volumes of DI water and the polystyrene microsphere suspension, while maintaining the volume fraction f of the microspheres in solution close to 0.1 [22]. A pre-calculated volume of this liquid phantom was pipetted onto the surface of the solid Rhodamine-RTV matrix, thereby creating a top layer of specified thickness (z_1).

The absorption coefficients of the top layer at the excitation and emission wavelength were taken to be that of water, while those of the bottom layer were obtained by measuring the transmission of a 1.43 cm thick RTV slab in a standard spectrophotometer (DU 800, Beckman Coulter, Fullerton, CA). The fluorescence absorption coefficient for the top layer was calculated from the transmission measurement of a stock solution of POPOP (diluted to 10 μM with DI water) in the spectrophotometer using a 1 cm path-length cuvette. For the bottom layer, a similar transmission measurement was made on a 2.23 cm thick, clear, RTV slab that had Rhodamine-6G concentration of 5 μM, but contained no scatterer. It is to be noted that the above measurements isolated the fluorescence absorption coefficient (μ_{afx}) at each relevant wavelength, from the absorption coefficient (μ_{ax}) for each layer. The scattering coefficients and anisotropies for the scattering phantoms were obtained from Mie theory, as described previously [13, 22]. These values for the optical transport properties, fluorophore absorption coefficients, and the upper layer thickness provided all the simulation inputs needed to model the bi-layered tissue phantom, except for the fluorescence quantum yields. The quantum yield values were the only parameters freely scaled to match simulated predictions to experimental measurements, as described in Section 3.

The liquid-solid, bi-layered fluorescence phantoms were manufactured with different combinations of liquid top layer thicknesses (z_1) and POPOP concentrations, atop the same solid RTV-141 silicone bottom layer, to create four different tissue models. Table 1 lists the differences in the properties of the four tissue models, Tissue#1 – Tissue #4. The scattering and absorption coefficients for each individual layer of all four phantoms were kept constant. The values fluorescence absorption coefficients for Rhodamine-6G in RTV were measured to be 0.03 cm^{-1} and 0.007 cm^{-1} for absorption at 337.1 nm (the incident excitation) and 418 nm (the peak of POPOP emission, see next section), respectively.

Table 1. Differences in the four bi-layered tissue models used to validate the simulations.

Phantom	[POPOP] (μM); μ_{afx} @ 337.1 nm (cm^{-1})	z_1 (mm)
Tissue #1	0.60; 0.055	2.5
Tissue #2	1.20; 0.110	2.5
Tissue #3	0.35; 0.03	2.5
Tissue #4	0.35; 0.03	3.5

2.3. Instrumentation

A fiber-optic fluorescence spectrometer was employed to measure remitted fluorescence from the bi-layered tissue phantoms described above. This fiber-optic fluorescence spectrometer used a subset of instrumentation contained in a fluorescence lifetime spectrometer (FLS), which was described previously in detail [23]. Briefly, the FLS coupled a pulsed nitrogen laser (337.1 nm excitation wavelength; pulse-width 4 ns; VSL-337, Laser Science Inc., Franklin, MA) by a flip-mirror into a quartz optical fiber (the "source" fiber in Fig. 1; 600 μm diameter; 0.22 NA; SFS600/660N, Fiberguide Industries, Stirling, NJ) to deliver excitation light to the bi-layered phantom. Another identical optical fiber (the "detector" fiber in Fig. 1)

#8207 - $15.00 USD Received 19 July 2005; revised 2 September 2005; accepted 7 September 2005

collected fluorescence emission from the phantom surface which was optically filtered by a dichroic mirror and band-pass filters to remove excitation light, and delivered to the entrance

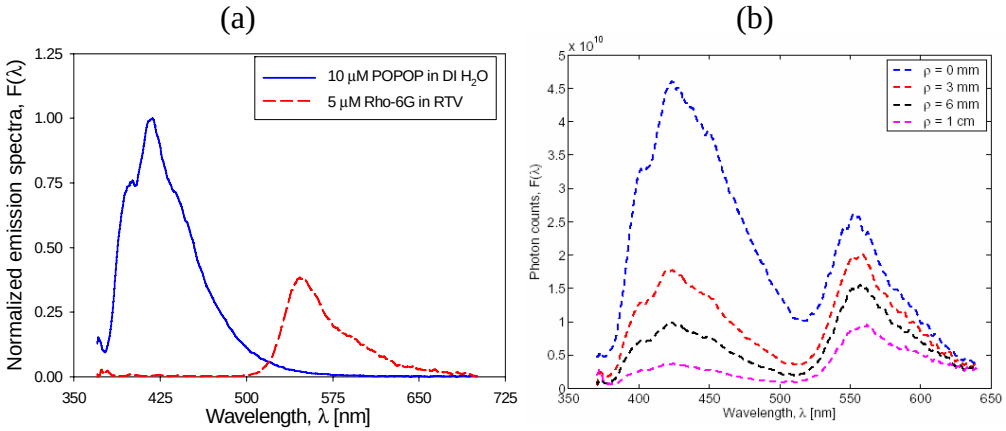

Fig. 2. (a) shows reference normalized (see text) fluorescence emission spectra of fluorophores POPOP in DI H_2O and Rhodamine-6G in RTV-141. (b) shows variations in the fluorescence emission spectra from the bi-layered tissue phantom (Tissue #1, Table 1) for different source-detector separations ρ.

slit of a spectrograph (MS125, Oriel Instruments, Stratford, CT) equipped with a gated, intensified charged coupled device (ICCD, Andor Technology, Belfast, Northern Ireland) at the exit port. (We note that although there was a distinct "source" and "detector" in these experiments, we could use the fiber-optic fluorescence spectrometer in a single fiber configuration, as well, wherein the "source" and "detector" fibers were one and the same [13].) The gate width of the ICCD was set to 275 ns and the gate was triggered by a delay generator that accounted for the transit time of light to reach the sample and back to the detector, relative to the emergence of each pulse from the laser. This scheme provided a means to minimize the presence of ambient light in the measured spectra [23]. Each measurement was an average of 50 laser pulses and these spectra were background corrected for any residual ambient light collected by subtraction of the measured ICCD response from an empty beaker (similar to that which housed the phantoms). The average laser power at the sample was 20 μJ /pulse. The spectral resolution of the instrument was found to be ± 3nm, while the pixel-pixel distance was 0.7 nm/pixel. All data shown here were first calibrated for both wavelength and absolute fluorescence intensity, as described previously [23] and then smoothed by a running average (nearest four neighbors) algorithm, leading to an overall resolution of ± 6 nm.

Figure 1 also shows the positioning apparatus that was designed to control the relative spatial orientation of the source and detector optical fibers. Identical micrometers M_1 and M_2 (SM13, Newport Corp., Irvine, CA; travel range 13 mm) in Fig. 1 allowed precise (± 2 μm) vertical alignment of the bi-layered phantom surface relative to the faces of the two optical fibers. This was achieved by first raising the phantom (with M_1) such that the liquid surface just touched the source fiber and by then lowering the detector fiber (with M_2) until it touched the liquid surface. The micrometer M_3 (SM13, Newport Corp., Irvine, CA; travel range 25 mm) enabled exactly the same precision control (± 2 μm) over the source-detector separation, ρ.

2.4. Data analysis: experiment

The accuracy of the Monte Carlo code was validated by comparing simulation predictions with experimental measurements on the bi-layered tissue phantoms in Table 1. The idea was to acquire spectra from the bi-layered tissue phantoms while systematically varying the

#8207 - $15.00 USD Received 19 July 2005; revised 2 September 2005; accepted 7 September 2005

source-detector separation, ρ, thereby altering the spatial sampling of the top relative to the bottom phantom layer. Altered sampling was quantified by analyzing the experimentally obtained fluorescence spectra to determine the fractional contribution from the fluorophore in each layer to the total detected fluorescence.

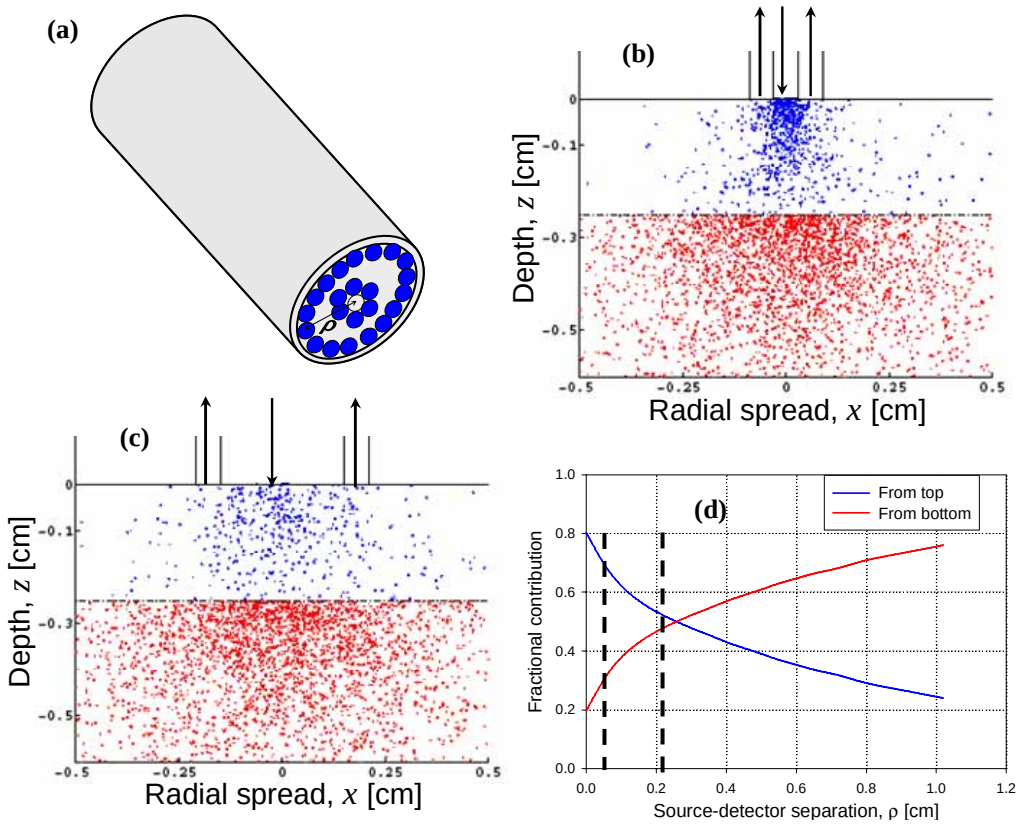

Fig. 3. (a) shows a schematic of the compound probe used in simulations (the central fiber is the source fiber). (b) and (c) depict cross-sectional views of the model tissue (Tissue #3, Table 1). The downward arrow indicates the source, while the upward arrows indicate the detectors. (d) shows the calculated fractional fluorescence contribution detected from each layer vs. ρ (as described in the text)

Figure 2(a) shows the normalized fluorescence emission spectra of 10 μM POPOP solution in DI H_2O (solid blue line) as well as the normalized emission spectrum 5μM Rhodamine-6G in RTV-141 (dashed red line), measured using the fiber-optic fluorescence spectrometer in a single fiber configuration. The emission spectrum of Rhodamine-6G in Fig. 2(a) was normalized using the peak value of the POPOP fluorescence emission. These two fluorophores were selected, in part, because they are spectrally distinct, as illustrated by the figure. Figure 2(b) shows remitted fluorescence spectra measured from the bi-layered tissue phantom Tissue #1 (Table 1) for four different source-detector separations, corresponding to different readings of the micrometer M_3 (Fig.1). The phantom spectra revealed two distinct, prominent spectral features, as expected. In Fig. 2(b), the blue line shows the emission spectrum from the phantom for $\rho = 0$ cm (single fiber geometry), the red line for $\rho = 0.3$ cm, the black line for $\rho = 0.6$ cm, and the magenta line for $\rho = 1$ cm. For increasing source-detector separation, there was an increase in the fluorescence emission intensity measured at 550 nm (Rhodamine-6G peak from the bottom layer) with a corresponding decrease at 420 nm (POPOP peak from the top layer). It was possible to determine, for each source-detector

#8207 - $15.00 USD Received 19 July 2005; revised 2 September 2005; accepted 7 September 2005

separation, the fractional contribution from the fluorophore localized either in the top or the bottom layer (i.e., POPOP or Rhodamine-6G) to the total detected fluorescence. The fractional contribution from POPOP to each measured spectrum was defined as the ratio of the area under the curve when the emission wavelength λ_{em} was bounded between 380 nm < λ_{em} < 510 nm to the total area under the curve (bounded by 380 nm < λ_{em} < 640 nm). Likewise, the fractional contribution from Rhodamine-6G was defined as the ratio of the area under the curve when the emission wavelength λ_{em} was bounded between 510 nm< λ_{em} < 640 nm to the total area under the curve. Hence, the sum of the fractional contributions was always unity, by definition.

2.5 Data analysis: simulations

Photon migration in the fluorescent bi-layered tissue phantoms described above was simulated computationally using the Monte Carlo code (each simulation used 10^7 photons). The diameters of the source and detector fibers used in the simulation were both set to 600 μm to match experimental conditions, while the numerical aperture in the simulation was set to unity so that the simulation counted every photon that escaped the tissue medium. Because the code stored the weighted 3-dimensional location of the spatial origin of fluorescence photons reaching each detection fiber placed on the tissue surface, it provided a means of quantifying the fractional fluorescence contributions predicted from each layer of the phantom. This enabled direct and quantitative comparisons between experimental measurements on bi-layered phantoms and simulation predictions for varying tissue morphology and fiber optic source-detector geometry.

This procedure is illustrated in Fig. 3 for Tissue #3 from Table 1, where simulation parameters were matched to experimental conditions. Figure 3(a) shows a schematic of the fiber-optic probe modeled by the simulations. The probe shown was comprised of a single, central "source" optical fiber (600 μm diameter) surrounded by two concentric annuli (600 μm thickness) of detector fibers, with mean annular radii ρ = 0.6 mm and ρ = 2.4 mm. Figs. 3(b) and 3(c), show the fluorescence detection that occurred for each of the detector annuli. Figure 3(b) corresponds to the detector annulus at ρ = 0.6 mm, while Fig. 3(c) shows it at ρ = 2.4 mm, from the center of the source fiber. These figures show the model tissue phantom in cross-section for those specific source-detector geometries, where each colored dot corresponds to the 2-dimensional spatial projection of the 3-dimensional spatial origin of a fluorescence photon that reached the corresponding detector fiber rings. Thus, blue dots show origins of fluorescence photons originating from POPOP in the top layer, while red dots show the origins of fluorescence photons emanating from Rhodamine-6G in the bottom layer. By counting these colored dots, we could determine the percentage of the detected fluorescence signal originating from fluorophores in the top and bottom layers. This fractional contribution is plotted in Fig. 3(d) as a function of the source-detector separation ρ, where the dashed vertical lines correspond to the data depicted in Fig. 3(b) and 3(c). Figure 3(d) reveals quantitatively how, for the same source configuration, increasing the source-detector separation ρ can yield an overall detected fluorescence signal that originates preferentially from deeper within the tissue phantom. For example, it can be seen that in ρ = 0.6 mm probe design 75% of the detected fluorescence arises from the fluorophore in the upper layer, while the contribution to the total fluorescence from the fluorophore in the upper layer falls to 56% for the ρ = 2.4 mm probe design.

3. Experimental validation of Monte Carlo Code

For the four bi-layered tissue phantoms described in Table 1, fluorescence emission spectra were measured experimentally and fractional fluorescence contributions from each layer were determined. Four corresponding bi-layered tissue models were constructed computationally, simulations were run, and fractional fluorescence contributions from each layer were calculated. Figure 4 compares experimentally measured results (circles) with predictions from the computational simulations (triangles), where the fractional fluorescence contribution

#8207 - $15.00 USD Received 19 July 2005; revised 2 September 2005; accepted 7 September 2005

from the top layer (blue lines) and that from the bottom layer (red lines) are plotted vs. source-detector separation, ρ. Figs. 4(a)-(d) correspond to the phantoms labeled Tissue #1-Tissue #4 in Table 1, respectively.

As mentioned previously, for each computational phantom model, the optical properties (μ_a, μ_s, g) and the fluorophore coefficients (μ_{afx}, τ_o) for each layer at each wavelength (excitation and emission), as well as the upper layer thickness (z_1), were obtained directly from experimental measurements. The quantum yields of POPOP and Rhodamine-6G were set to 0.8 and 0.7, respectively, for all models. The simulated fractional fluorescence contribution curves from these simulations were then normalized to match the experimentally measured value of the fractional contribution for the fluorophore in the upper layer (blue line) at ρ = 0.55 cm, for each phantom.

As seen in Figs. 4(a)-4(d), for both the experimental measurements as well as the simulated predictions, the fractional contribution to the total detected fluorescence from the fluorophore in the top layer (blue lines) decreased with increasing source-detector separation ρ, while the fractional fluorescence from the fluorophore in the bottom layer (red lines) increased. These trends in the fractional fluorescence contributions were expected since the photons reaching detectors farther away from the source penetrate deeper into the tissue medium, relative to photons reaching detectors closer to the source, as has been noted previously by other reports [24].

The overall agreement between simulation and experiment was very good. For $\rho > 0.1$ mm, simulations and experiments agreed to better than 3% of each other for all four phantoms. Further, the accuracy of the simulation predicted cross-over point (the point where the blue and red lines cross) relative to experiment was better than 2% for each of Tissues #1, Tissue #3 and Tissue #4. The poorest agreement between simulation prediction and experiment occurred for the smallest experimentally achievable source-detector separation (ρ = 0.06 cm), where the agreement between the simulations and experiment was closer to 8% in Figs. 4(a) and (d). This was attributed to the fact that at this source-detector separation, the "source" and "detector" fibers touched each other in the experiments and this contact could have led to either of the fiber axes being deviated slightly from the normal to the tissue surface.

The simulations and experiments also predicted intuitively understandable trends for the value of the cross-over point between red and blue curves, i.e., the source-detector separation value for which the fractional contribution from the top and bottom layers were equal (0.5 or 50%), vs. changes in tissue properties. The cross-over point for Tissue #1 (Fig. 4a) must be less than that for Tissue #2 (Fig. 4b), given that Tissue #2 had an increased concentration of POPOP in the top layer (leading to a larger value for the fluorescence absorption coefficient) relative to Tissue #1. Therefore, for a given ρ, the fractional fluorescence from POPOP for Tissue #2 would be higher than that of Tissue #1, since there would be a greater number of fluorescence photons generated in the upper layer of Tissue #2 relative to Tissue #1. Similarly, an increased upper layer thickness in Tissue #4 (Fig. 4(d)) relative to Tissue #3 (Fig. 4(c)) yielded an overall increased sampling of fluorescence from the upper layer in Tissue #4, thereby causing the fractional fluorescence from POPOP to be larger in Tissue #4 vs. Tissue #3.

We note that excellent agreement between the simulations and the experiments for each of the bi-layered tissue phantoms is indicative of the validity of the computational model to provide a quantitative means for estimating fluorescence transport in bi-layered tissue models. We also note that the analysis of remitted fluorescence from such bi-layered tissue models by calculating fractional fluorescence contributions with varying source-detector separations provides a simple yet robust technique that is sensitive to changes in the upper-layer thickness, as well as the concentrations of fluorophores in either layer. In the next section, we utilize the code to simulate fluorescence from bi-layered human epithelial tissue models and examine the influence of tissue optical properties and source-detector configurations on the

#8207 - $15.00 USD Received 19 July 2005; revised 2 September 2005; accepted 7 September 2005

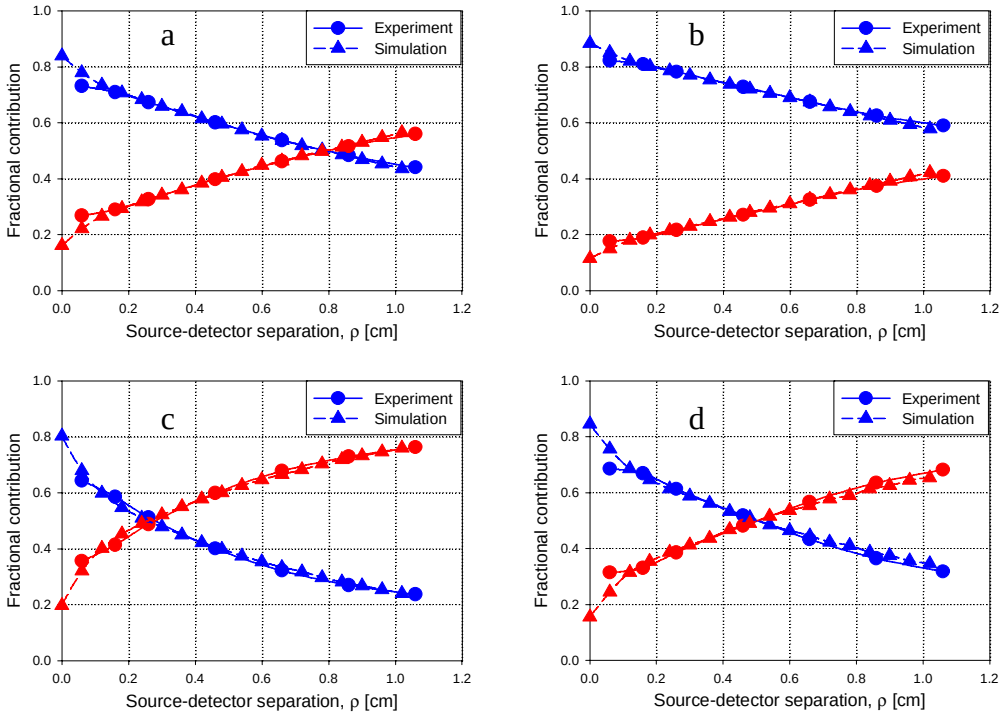

Fig. 4. Comparisons of the experiments (circles) with simulations (triangles) for the bi-layered tissue phantoms listed in Table 1. Fig. 4(a)-4(d) correspond to Tissue#1 -Tissue #4, respectively. In each figure, blue lines indicate fractional fluorescence contributions from the top layer, while red lines show contributions from the bottom layer.

signals detected via point spectroscopy and imaging modalities, for time-gated (fluorescence lifetime), time-integrated (fluorescence intensity), and frequency domain instrumentation.

4. Results: demonstration of code capabilities

4.1. Numerically modeling in vivo *data from human tissues*

Table 2. Parameters used in normal (CTM1) and pre-cancerous (CTM2) human tissue models in Section 4. The anisotropy coefficients of both layers were fixed at 0.9 for all simulations.

Colon Tissue Model (CTM)		CTM1 (normal)	CTM2 (adenoma)
Optical Transport Coefficients (cm-1)	$^1\mu_{ax}$, $^1\mu_{am}$ (absorption)	12,3	20,10
	$^1\mu_{sx}$, $^1\mu_{sm}$ (scattering)	200,90	120, 70
	$^2\mu_{ax}$, $^2\mu_{am}$ (absorption)	12,3	12,3
	$^2\mu_{sx}$, $^2\mu_{sm}$ (scattering)	200,90	200,90
Mucosal thickness, z_1 (μm)		400	700
Fluorophore Absorption (cm-1)	$^1\mu_{afx}$	0.5	0.5
	$^2\mu_{afx}$	1.5	1.0
Quantum Yields (cm-1)	$^1\Phi_{QY}$	0.05	0.05
	$^2\Phi_{QY}$	0.3	0.1

#8207 - $15.00 USD Received 19 July 2005; revised 2 September 2005; accepted 7 September 2005

A motivation for the development of a computational model for time-resolved fluorescence transport in bi-layered tissues was provided by clinical fluorescence measurements of human colonic tissues *in vivo* in a previous study [3]. Figure 5(a) plots representative fluorescence decays measured from a normal tissue site (blue line) and an adenomatous (pre-cancerous) polyp (red line), showing that normal tissues had longer lived endogenous fluorescence vs. adenomatous tissues. These tissue data were simulated computationally by constructing a

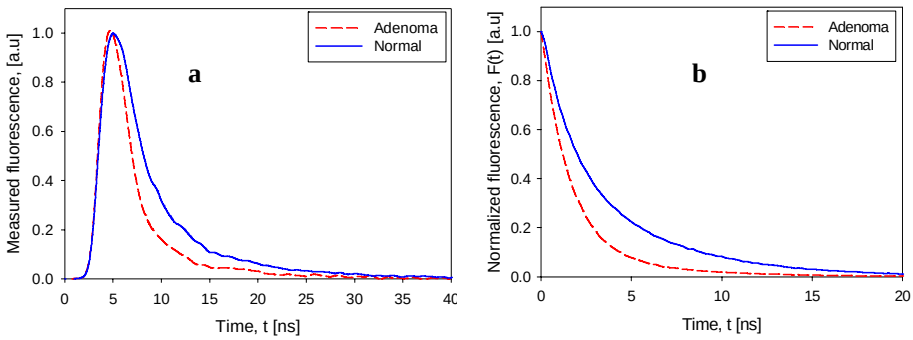

Fig. 5. Time-resolved fluorescence decays measured *in vivo* are shown in (a), while computational simulations are shown in (b). Normal tissues are indicated by the solid blue lines, while pre-cancerous adenomatous tissues are shown by the red dashed lines.

numerical bi-layered model of human colonic tissue, with NADH as the fluorophore in the upper (mucosal) layer and collagen as the fluorophore in the bottom (submucosal) layer [20]. Table 2 lists the set of tissue optical and fluorophore coefficients used to create the normal colon tissue model (CTM1) and adenomatous colon tissue model (CTM2). These numerical values were gathered from several different studies [20]. These simulations used a single optical fiber to deliver and collect light from the mucosal surface of the tissue, matching the clinical experiments [3] and thereby enabling direct, quantitative comparisons between the simulated fluorescence decays and the clinically measured fluorescence traces.

The results of time-resolved fluorescence predictions from the simulations are shown in Fig. 5(b) with the blue line corresponding to normal colon tissue model and the red line corresponding to an adenomatous colon tissue model. These results demonstrated that variations in optical transport coefficients (absorption and scattering) alone could not account for the fluorescence decay differences detected between tissue pathologies *in vivo*. However, variations in fluorescence decay times as large as those detected clinically between normal and pre-cancerous tissues (~2 ns) could be accounted for by simulated variations in tissue morphology (specifically, the upper layer thickness z_1) and biochemistry (the fluorophore absorption coefficient and quantum yield of the fluorophore in the bottom layer), even when intrinsic fluorophore lifetimes were held constant [20]. Because 85% of all human cancers occur in epithelial tissues, the ability to quantitatively simulate light transport in bi-layered epithelial tissues could be useful for human cancer prevention via early detection of pre-cancerous tissues, by enabling the development of quantitative optical diagnostic spectroscopy and imaging methods.

#8207 - $15.00 USD Received 19 July 2005; revised 2 September 2005; accepted 7 September 2005

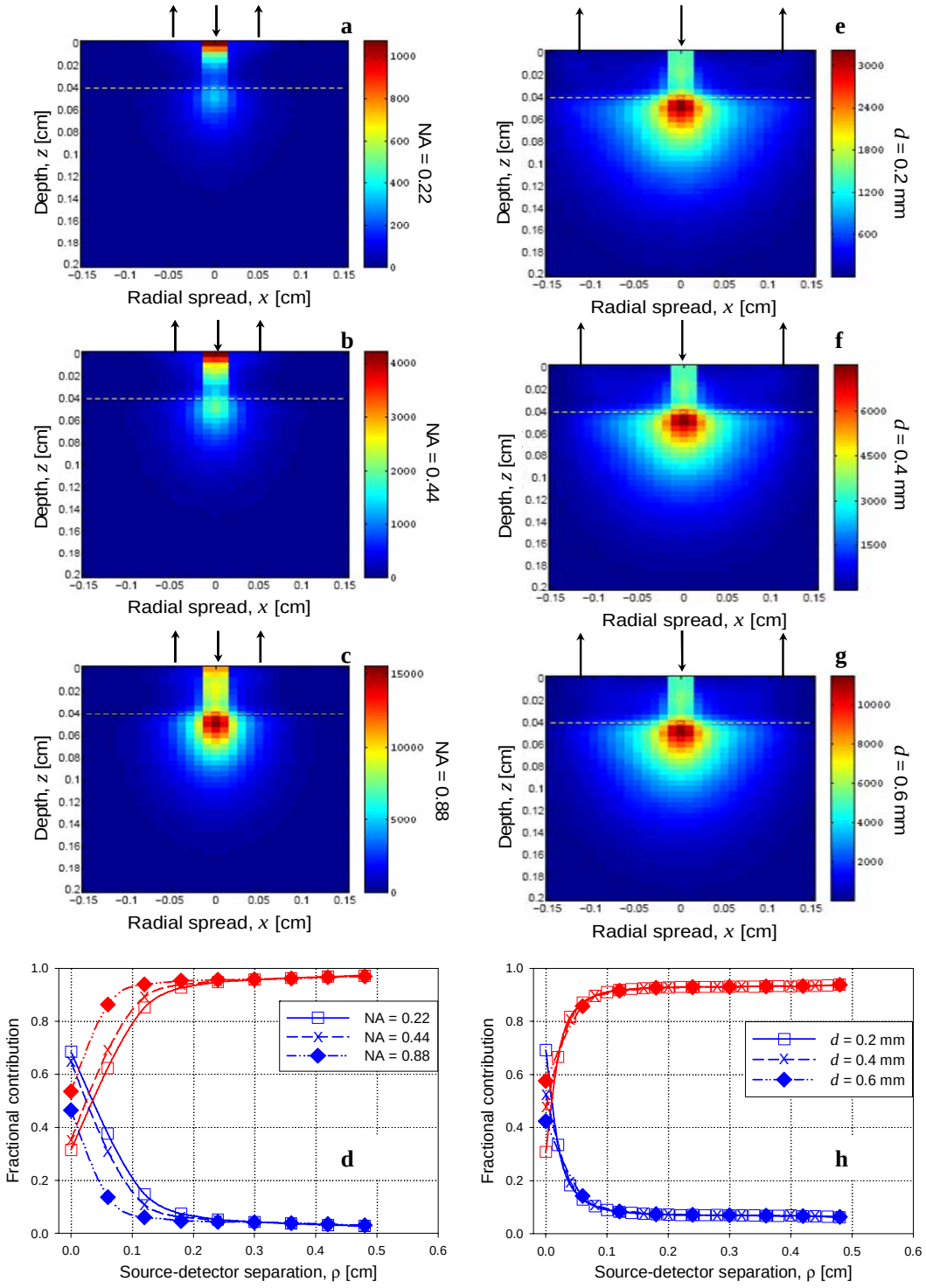

Fig. 6. (a)-(c) show the projected 2-d map of fluorescence photons reaching the detector for varying detector numerical apertures, while (e)-(f) show that for varying detector diameters *d* (see text). Figs. (d) and (h) quantify these data as fractional fluorescence contributions vs. source-detector separation ρ for the top layer (blue lines) and the bottom layer (red lines). These simulations modeled normal human colon tissue (CTM1, Table 2).

#8207 - $15.00 USD Received 19 July 2005; revised 2 September 2005; accepted 7 September 2005

4.2. Predicting the efficiency of fiber-optic waveguide configurations

A significant advantage of having validated computational simulations that can predict light transport in turbid media is the ability to quantitatively examine experimental design configurations (for example, to test different light delivery and collection systems and quantify how these configurations will affect detected light for different tissue models) without requiring the costly and time-consuming manufacturing and testing of these designs. Here, we specifically examine the effect of varying detector-fiber numerical apertures and diameters on both the origin of detected fluorescence, as well as the fractional fluorescence contributions from the two-layered colon tissue model CTM1 (Table 2).

Figures 6(a)-(c) show the 2-dimensional projection (in the *x*-*z* plane) of the 3-dimensional spatial origin of the fluorescence photon number density that reached the detector-fiber annulus (indicated by the upward arrows), for each of three values of the detector-fiber numerical aperture. In these images, the dashed yellow lines indicate the upper-layer thickness (400 μm) while the downward arrows indicate the source-fiber. The diameter of the detector fiber annuli, as well as the source-detector separations in these figures, were all fixed at 600 μm. Figures 6(a)-(c) show these data when the numerical aperture (NA) of the detection fiber was 0.22, 0.44 and 0.88, respectively. As seen from Fig. 6(a)-(c), increasing numerical apertures of the detection fibers increased the amount of fluorescence detected from the lower layer and thus the number of fluorescence photons generated there increased with increasing numerical aperture. Figure 6(d) quantified this in terms of the fractional fluorescence contributions from each layer with varying source-detector separation. The blue lines in Fig. 6(d) represent the fractional fluorescence contribution from NADH (in the top layer) while the red lines indicate the contribution from collagen (in the bottom layer) – the squares, the crosses, and the diamonds represent the fractional contributions when the detector NA = 0.22, 0.44, and 0.88, respectively. As seen in Fig. 6(a)-(c), the blue curves in Fig. 6(d) show the increased sampling of fluorescence from the upper layer with decreasing detector numerical apertures.

Figures 6(e)-(g) show the 2-dimensional projection (in the *x*-*z* plane) of the 3-dimensional spatial origin of the fluorescence photon number density that reached the detector-fiber annulus (indicated by the upward arrows), for each of three values of the detector-fiber diameter. In these images, the dashed yellow lines indicate the upper-layer thickness (400 μm) while the downward arrows indicate the source-fiber. The source-detector separation in these figures was fixed at 1.2 mm, while the detector numerical aperture was set at 1.00. Figures 6(e)-(g) show data when the diameters *d* of detection fiber annulli were 200, 400 and 600 μm, respectively. As seen from Fig. 6(e)-(g), the increased diameters of detection fibers did not significantly change the amount of fluorescence detected from either layer and although the total number of fluorescence photons generated in each layer increased with increasing diameter, as expected. The selective sampling of fluorescence in the upper (or lower) layer for all the three detector diameters converged to identical values for source-detector separations greater than ρ = 0.6 cm, as seen in Fig. 6(h), which quantified the fractional fluorescence contributions of each layer with varying source-detector separation for the three different detector diameters. As before, the blue lines in Fig. 6(h) represent the fractional fluorescence contribution from NADH (in the top layer), while the red lines indicate the contribution from collagen (in the bottom layer) – the squares, the crosses, and the diamonds represent the fractional contributions when the detector diameters were d_1 = 200 μm, d_1 = 400 μm and d_1 = 600 μm, respectively.

4.3. Visualizing time-resolved and time-gated tissue fluorescence

Figures 7(a)-(d) show perspective views of the spatial origin of fluorescence photons for CTM1 (Table 2) in 3-dimensions. All figures indicate the central source fiber via the blue tube, while the detector annuli (surrounding the source fiber) are indicated by orange tubes. Figures 7(a) and 7(c) show time-gated snapshots (gate width of 0.1 ns, gate-delay of 0.5 ns) of the spatial origin of fluorescence photons reaching detector fibers, whose edges were placed at

#8207 - $15.00 USD Received 19 July 2005; revised 2 September 2005; accepted 7 September 2005

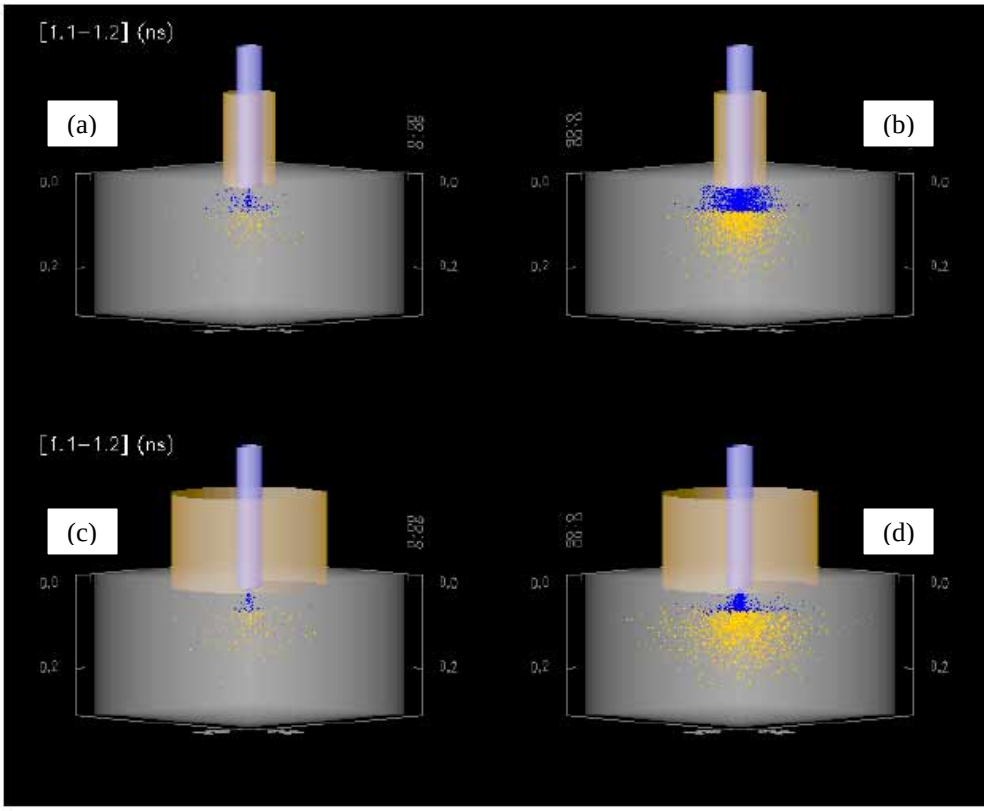

Fig. 7. For the normal colon tissue model (CTM1), 3-dimensional visualizations showing the spatial origins of fluorescence photons reaching the detectors (orange tubes). The excitation was delivered via a source-fiber (blue tube). (a) and (c) show time-gated snapshots (between 1.1- 1.2 ns), while (b) and (d) show time-integrated data. The multimedia movie shows the data from 0-6 ns (2.21MB).

ρ = 0.12 cm (Fig. 7(a)) and at ρ = 0.42 cm (Fig. 7(c)) from the center of the source (which was a delta-function in time). The diameters of the source and detector fibers were 600 μm in these simulations.

Figures 7(b) and 7(d) show the time-integrated spatial origins of fluorescence photons reaching the detector rings from the onset of the incident delta-function excitation pulse. These visualizations allow us to perceive in 3-dimensions the fractional fluorescence contribution from each layer that can be detected by varying source-detector geometries in simulations. The embedded multimedia movie shows the time-gated (Fig. 7(a) and 7(c)) and time-integrated (Fig. 7(b) and 7(d)) origins of the fluorescence photons reaching the detector fiber annuli, with a frame increment of 100 ps after the incident pulse (at t = 0). These simulations have the potential to estimate optimal parameters for time-gated vs. time-integrated imaging in these turbid media.

It is also possible to use the 3-dimensional simulations of time-resolved remitted tissue fluorescence to visualize the detected time-gated and time-integrated intensity patterns that would be observed on any 2-dimensional plane, including the tissue surface. For the model colon tissues in Table 2, Fig. 8(a) shows the simulated surface intensity data for CTM1, while Fig. 8(b) shows data for CTM2 [20]. Figures 8(a) and 8(b) show the remitted fluorescence intensity at the surface 0.2 ns after the incident delta-function pulse excitation. As can be seen, in CTM2 the increased mucosal layer thickness and the decreased submucosal fluorophore absorption and quantum yield caused alterations in both the spatial and temporal surface

#8207 - $15.00 USD Received 19 July 2005; revised 2 September 2005; accepted 7 September 2005

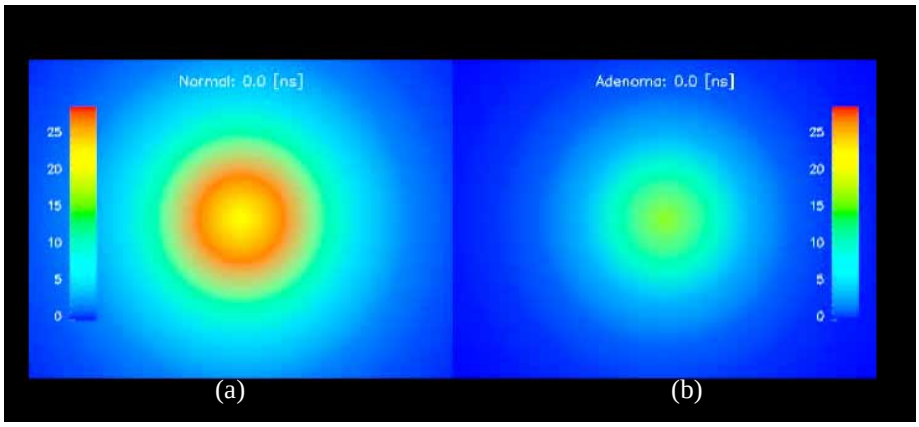

Fig. 8. Surface fluorescence intensity maps showing the remitted tissue fluorescence for the two simulated colon tissue models in Table 2. (a) shows the surface of a normal tissue (CTM1), while (b) shows that of an adenomatous tissue (CTM2). The multimedia movie shows the data from 0-6 ns (2.31MB).

fluorescence intensity patterns, relative to CTM1. Thus, the bi-layered computational model may be used to quantitatively simulate both point-spectroscopy applications using fiber-optic waveguides, as well as optical imaging modalities for tissue diagnostics. Each frame of the embedded multimedia movie shows the total fluorescence intensity detected at each detection-fiber annuli for both tissue models.

4.4. Equivalence of steady-state, time-resolved, and frequency-domain analysis

As described above, the Monte Carlo simulation stored the weighted local 3-dimensional spatial origins of fluorescence photons that reached each detector fiber ring annulus (as shown in Fig. 3), which then permitted calculation of the fractional fluorescence contributions from each layer as a function of varying source-detector separation, for every simulation run. This method of calculating the fractional fluorescence contributions did not consider the temporal dependence of the remitted fluorescence and thus could be called the steady-sate method for calculation of the fractional fluorescence contribution from each layer.

However, each simulation also stored the time-resolved fluorescence detected within each annular detector ring. Moreover, within a simulated run, the intrinsic fluorophore lifetime of each fluorophore was constant. Thus, it is possible to estimate the fractional fluorescence contribution from each fluorophore at each detector location by fitting the simulated time-resolved fluorescence data $F(t)$ to a weighted bi-exponential decay, where each exponential had a distinct decay constant τ_i (which was the lifetime of each fluorophore input to the tissue model), i.e. $F(t) = \alpha_1 \exp(-t/\tau_1) + \alpha_2 \exp(-t/\tau_2)$. Once α_1 and α_2 were determined via a least-squares curve fitting technique, the fractional fluorescence from layer i was obtained by calculating the fractional area under $F(t)$ from the contribution of the i^{th} fluorophore, as has been described previously [20, 25]. This method could be called the time-resolved method for calculating the fractional fluorescence contribution from each fluorophore directly from the raw, simulated time-resolved fluorescence data.

Further, since each simulation provided us with the time-resolved fluorescence measured at each detector location, it is possible to calculate the fractional fluorescence contributions of each fluorophore by performing analysis identical to the time-resolved method, but in the frequency-domain. As has been discussed previously [25], frequency-domain approaches to measuring and analyzing light transport in turbid media provide an alternative means to time-domain techniques, while retaining the richness of information available via fluorophore lifetime spectroscopy. Thus, we could analyze the fractional contributions from each fluorophore by frequency-domain analysis of the simulated time-resolved data by first

#8207 - $15.00 USD Received 19 July 2005; revised 2 September 2005; accepted 7 September 2005

transforming the simulated time-resolved fluorescence $F(t)$ (at each detector location) via an FFT into a complex, frequency dependent response $f(\omega)$. The phase delay of this transformed signal (i.e. $\tan^{-1}\{\mathrm{Re}[f(\omega)] / \mathrm{Im}[f(\omega)]\}$) was then fit to the phase calculated from the complex, Fourier transformed, weighted bi-exponential decay (as described above) to determine the values α_1 and α_2 that best matched the simulated data [25]. These values then allowed calculation of the fractional fluorescence contributions from each fluorophore. This technique can be called the frequency-domain method to obtain fractional fluorescence contribution from each fluorophore.

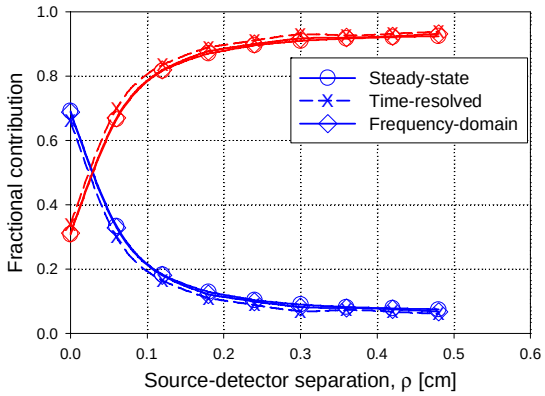

Fig. 9. Equivalence of analyzing fractional fluorescence contributions for a bi-layered normal colon tissue model (CTM1, Table 2) via steady-state (circles), time-resolved (crosses), or frequency-domain (diamonds) techniques. Blue lines show fractional contributions from the fluorophore in layer 1, while the red lines show that from the fluorophore in layer 2.

Figure 9 shows the equivalence of three described methods in calculating the fractional fluorescence contributions from each fluorophore for a bi-layered normal colon tissue model (CTM 1, Table 2). As in previous figures, the blue lines indicate the fractional fluorescence contribution from the fluorophore in layer 1 (the upper layer), while the red lines show that for layer 2 (the lower layer). Here, the circles show the analyses using the steady-state technique, the crosses correspond to the time-resolved technique, while the diamonds show the data obtained using the frequency-domain technique. The simulations shown here correspond to source and detector fibers with 600 μm diameters and numerical apertures of unity. The excellent agreement among the 3 methods indicates the equivalence of steady-state, time-resolved, and frequency-domain analyses, as well as the utility of the computational model described and validated here to accommodate a broad variety of experimental methodologies.

5. Conclusions

A novel Monte Carlo code for time-resolved photon migration simulations of light propagation in bi-layered models of biological tissues was presented and experimentally validated. The broad utility of this numerical method was illustrated via several applications in clinical optical diagnostics, including: (i) Applications to quantitative fluorescence sensing in human epithelial (colon) tissues *in vivo*; (ii) Visualization of the 3-dimensional spatial origins of fluorescence photons in tissues vs. variations in optical waveguide design; (iii) Extensions from tissue surface point spectroscopy to surface imaging modalities, for both time-gated (fluorescence lifetime) and steady-state (fluorescence intensity) measurements; (iv) Illustration of the flexibility of the computational approach to quantitatively interpret experimental measurements employing either time- or frequency-domain instrumentation.

#8207 - $15.00 USD Received 19 July 2005; revised 2 September 2005; accepted 7 September 2005

Acknowledgments

The authors wish to thank John Valenzuela and Manoj Rajagopalan for providing technical support and James Scheiman for many helpful discussions. This research was supported by grants from the National Institutes of Health to M.-A.M. (NIH RR-020214 and NIH CA-114542).

#8207 - $15.00 USD Received 19 July 2005; revised 2 September 2005; accepted 7 September 2005